



# Comparative study about the results of HAZ physical simulations on different high-strength steel grades

J. Kovács<sup>1</sup> · M. Gáspár<sup>1</sup> · J. Lukács<sup>1</sup> · H. Tervo<sup>2</sup> · A. Kaijalainen<sup>2</sup>

Received: 8 September 2023 / Accepted: 2 February 2024 / Published online: 24 February 2024  
© The Author(s) 2024

## Abstract

With continuous improvements, structural steels are available in even higher strength grades above 1000 MPa yield strength. As the great majority of these steels are used in welded structures, their weldability needs to be taken into account. Several factors can cause difficulties during welding of these steels, but in this paper the softening behavior and the toughness characteristics of the heat-affected zone (HAZ) are examined. As the critical parts of the HAZ in a real welded joint are relatively small, their investigating ability is limited. However, the physical simulation provides a way of evaluating specimens made from a given material to produce the specified HAZ areas in a suitable size range for subsequent testing. In this research work, three different strength categories of high-strength structural steels (with yield strength of 960 MPa, 1100 MPa, and 1300 MPa) are investigated by physical simulation. In the case of different technological variants of gas metal arc welding (GMAW) process, the effect of the cooling time  $t_{8/5}$  is investigated in different HAZ subzones considered to be critical. The thermal cycles were determined according to the Rykalin 3D model. The investigated cooling times were  $t_{8/5} = 5$  s, 15 s, and 30 s. The properties of the selected coarse-grained, intercritical and intercritically reheated coarse-grained zones are analyzed by laser scanning microscope, scanning electron microscope, hardness test, and instrumented Charpy V-notch impact toughness test. Furthermore, additional investigation like JMatPro calculations, electron backscatter diffraction measurements, and prior austenite grain size calculation were carried out. As a result of the tests, the investigated heat-affected subzones indicated higher sensitivity to the welding heat input compared to conventional structural steels. Overall, the results of the tests show that the application of shorter  $t_{8/5}$  cooling time can be beneficial for the investigated high-strength steel grades, since significant toughness reduction and the risk of softening occur in the whole cooling time range.

**Keywords** High-strength steel · Physical simulation · Heat-affected zone · Instrumented impact test · Electron Backscatter Diffraction (EBSD)

## 1 Introduction

Steels are one of the most important structural materials worldwide, and therefore, the developments of structural steel have a global industrial impact [1]. By selecting the appropriate chemical composition, the rolling conditions, and heat treatment, the steel grade is obtained of a yield strength even above 1300 MPa. Generally, the high-strength categories of structural steels are produced by quenched and tempered process with a final microstructure of martensite [2, 3]. The other production method is thermomechanical rolling process, which nowadays can also be used to produce thick plates with a yield strength of 1100 MPa. These types of high-strength steels (HSS) are used primarily in construction cranes, boom trucks, and other heavy-duty components, but despite that steels with yield strength up to 1300 MPa

✉ J. Kovács  
judit.kovacs@uni-miskolc.hu  
M. Gáspár  
marcell.gaspar@uni-miskolc.hu  
J. Lukács  
janos.lukacs@uni-miskolc.hu  
H. Tervo  
henri.tervo@oulu.fi  
A. Kaijalainen  
antti.kaijalainen@oulu.fi

<sup>1</sup> Institute of Material Science and Technology, University of Miskolc, 3515 Miskolc-Egyetemváros, Hungary

<sup>2</sup> Materials and Mechanical Engineering, Centre for Advanced Steel Research, University of Oulu, P.O Box 4200, 90014 Oulu, Finland

have been commercially available for years, they are rarely used [4, 5]. The high-strength steels can offer higher lifting and load capacity, higher wear resistance, and improved machinability [6]. The use of high-strength steel materials would facilitate in the reduction of self-weight of structures and associated handling, fabrication, transportation costs, and erection time [7]. As it was mentioned, these steels have been available in the market in years, but it should be noted, however, that the steels of yield strength above 1000 MPa are not mentioned in the current standards. This is due to the fact that these steels are relatively new materials for construction, and require testing, determining the weldability, and developing the welding technology [4].

When producing durable structures from the steel, weldability is an important material property because most constructions require welding in some point of the production chain [1]. As it is well known, welding modifies the mechanical properties by microstructural changes determined by the heat input and the cooling history [6]. The changes are especially prominent in the heat-affected zone (HAZ) of the welded joints [8]. During the welding of high-strength steels, the largest weldability problems can be caused by the unfavorable changes of the original microstructure. In the HAZ, both hardened and softened areas can be found [9, 10]. When the HAZ of conventional structural steels is examined, the coarse-grained zone is considered the most critical one in terms of the toughness properties. In the case of high-strength steels, the intercritical zone can be also similarly disadvantageous due to the higher carbon equivalent and the possible formation of local brittle zones (LBZ). In multipass welded joints, the unfavorable microstructural changes of both abovementioned zones (grain growth and

brittle microstructure at grain boundaries) can occur in the intercritically reheated coarse-grained zone, which is supposed to be the region of the whole welded joint with the lowest toughness [11–13].

The aim of the present research is to provide a detailed characterization (microstructure, hardness, toughness) of the HAZ of S960QL, S1100M, and S1300QL high-strength steels and to analyze the effect of welding parameters during the application of the gas metal arc welding (GMAW) technology. The idea was to analyze and compare the HAZ behavior of the latest and less frequently used steel categories (S1100M, S1300QL) with the relatively well-known S960QL grade. The properties of the subzones are investigated as a function of  $t_{8/5}$  cooling time by the application of physical simulation.

## 2 Experimental work

### 2.1 Investigated materials

During our research work, three different structural steels from different strength categories were examined. The investigated materials were as follows: Strenx 960 E (S960QL), alform plate 1100 M x-treme (S1100M) and an ultra-high-strength steel with 1300 MPa of yield strength (S1300QL). The mechanical properties and the chemical compositions of the three base materials are summarized in Tables 1 and 2, respectively. The data in the tables are according to the material certificates, except in the case of the S1300QL base material, which case due to the lack of material certificate,

**Table 1** Mechanical properties

| Base materials | Thickness, mm | Hardness, HV10 | $R_{p0.2}$ , MPa | $R_m$ , MPa | $A_5$ , % | CVN, J (at $-40\text{ }^{\circ}\text{C}$ ) |
|----------------|---------------|----------------|------------------|-------------|-----------|--|
| S960QL         | 15            | 340            | 1014             | 1053        | 14        | 161  |
| S1100M         | 15            | 394            | 1193             | 1221        | 11.6      | 88   |
| S1300QL        | 10            | 468            | 1300             | 1560        | 12        | 78   |

**Table 2** Chemical compositions

| Chemical compositions, weight% |       |       |       |       |        |        |        |       |
|--------------------------------|-------|-------|-------|-------|--------|--------|--------|-------|
| Base materials                 | C     | Si    | Mn    | P     | S      | Cr     | Cu     | Ni    |
| S960QL                         | 0.17  | 0.23  | 1.23  | 0.011 | 0.001  | 0.2    | 0.01   | 0.04  |
| S1100M                         | 0.13  | 0.32  | 1.62  | 0.009 | 0.0015 | 0.63   | 0.047  | 0.32  |
| S1300QL                        | 0.23  | 0.45  | 1.86  | 0.012 | 0.001  | 0.85   | 0.093  | 2.43  |
| Chemical compositions, weight% |       |       |       |       |        |        |        |       |
| Base materials                 | Mo    | V     | Ti    | Al    | Nb     | Zr     | B      | N     |
| S960QL                         | 0.588 | 0.041 | 0.004 | 0.061 | 0.017  | N/A    | 0.001  | 0.002 |
| S1100M                         | 0.62  | 0.066 | 0.011 | 0.035 | 0.037  | N/A    | 0.0014 | N/A   |
| S1300QL                        | 0.360 | 0.030 | 0.002 | 0.063 | <0.001 | <0.001 | N/A    | N/A   |

material tests and chemical analysis were made in the University of Miskolc.

From the data in Table 2, it can be seen that the Ni content increases significantly as the strength of the tested steels increases. It is also observed that these steel grades have low levels of contaminants. Based on the chemical compositions, the carbon equivalents were determined according to EN 10025–1:2004: E standard [14]. All the calculated carbon equivalent values can be seen in Table 3, which are increasing by the strength level in terms of the selected steel grades.

## 2.2 Physical simulation

The programs for the performed physical simulations were written by manual programming (instead of using automatic software settings), using time–temperature points calculated by taking into account the temperature-dependent physical properties. The aim of the selection of the peak temperature of the thermal cycles to be investigated was to produce the areas with the lowest toughness in the HAZ; thus, the coarse-grained (CGHAZ), intercritical (ICHAZ), and intercritically reheated coarse-grained (ICCGHAZ) zones were selected. Samples were heated to peak temperatures of 775 °C for the ICHAZ simulation and 1350 °C for the CGHAZ simulation and the two peak temperatures were applied simultaneously for the ICCGHAZ simulation. The selection of the peak temperature for ICHAZ simulations was based on literature [15, 16] and former investigations [13] considering a temperature, which can be in the intercritical range of the three steels. In order to simulate a low, a medium, and a high heat input in the case of gas metal arc welding process, three different cooling times were set during the tests. On this basis, the chosen cooling times were as follows:  $t_{8/5}$  = 5 s, 15 s, and 30 s. The parameters for the HAZ simulations are shown in Table 4.

The dimensions of the test specimens used during the physical simulation experiments were determined according to the recommendations of the Gleeble manual. The dimensions of the specimens were 10 mm × 10 mm × 70 mm. The K(NiCr-Ni) thermocouples were resistance welded to the specimens before starting the simulations. During the simulation, the process is controlled based on the temperature data provided by the thermocouples. The structure of the Gleeble workspace with the specimen is shown in Fig. 1.

**Table 3** CEV and CET values

| Base materials | CEV, % | CET, % |
|----------------|--------|--------|
| S960QL         | 0.54   | 0.36   |
| S1100M         | 0.68   | 0.39   |
| S1300QL        | 0.956  | 0.56   |

**Table 4** Parameters for the different heat-affected zone simulations

| Heat-affected zone areas                | Peak temperature, °C |              | $t_{8/5}$ cooling time, s |
|---|----------------------|--------------|---------------------------|
|   | $T_{\max 1}$         | $T_{\max 2}$ |                           |
| Coarse-grained                          | 1350                 | -            | 5, 15, 30                 |
| Intercritical                           | 775                  | -            | 5, 15, 30                 |
| Intercritically reheated coarse-grained | 1350                 | 775          | 5, 15, 30                 |

For each thermal cycle, a uniform preheating and inter-pass temperature of 150 °C was set. The tests were carried out in vacuum, thus providing protection against oxidation and decarbonization. The programmed thermal cycles for CGHAZ and ICHAZ areas are shown in Figs. 2 and 3, respectively.

For the simulations of ICCGHAZ areas, the combination of the CGHAZ and ICHAZ thermal cycles was used. Between the thermal cycles from 200 °C, forced cooling was used (until 150 °C), followed by 5 s of holding time (at 150 °C). For a better transparency, only one of the programmed ICCGHAZ thermal cycle is shown in Fig. 4.

## 3 Results and discussion

### 3.1 Microstructural investigation

After the simulations, each specimen was cut in the middle of the HAZ along the thermocouples for further material testing. As a first step, JMatPro calculations were performed and laser scanning confocal microscope (LSCM, Keyence VK-X200) images were taken. The LSCM images of the fine-grained different base materials in delivery

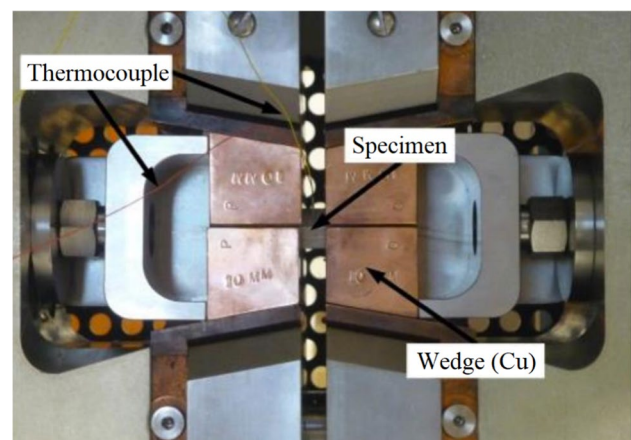


**Fig. 1** Gleeble workspace with the specimen

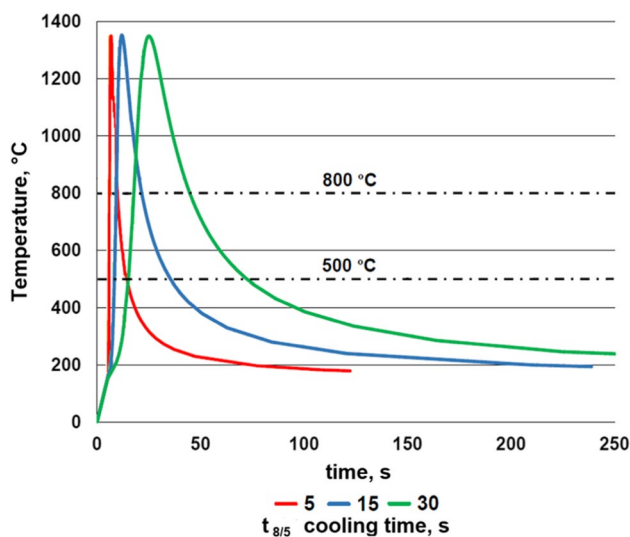


Fig. 2 CGHAZ thermal cycles

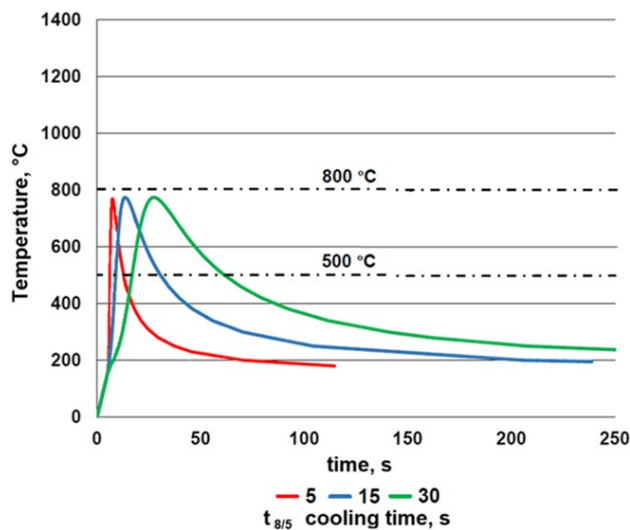


Fig. 3 ICHAZ thermal cycles

condition can be seen in Fig. 5. The specimens were etched by 3%  $\text{HNO}_3$  (Nital).

The microstructure of CGHAZ, ICHAZ, and ICCGAZ of the three different materials belonging to the applied cooling times are shown in Figs. 6, 7, and 8. Figs. 6, 7, and 8 show images of S960QL in the first column, S1100M in the second column and S1300QL in the third column. In the first row, the cooling time used during the tests is 5 s and 30 s in the second row.

In Fig. 6, the images of the S960QL show that prior austenite grain size in the coarse-grained zone has increased significantly compared to the size of the original grains as a result of heating to near solidus temperature. Fundamentally

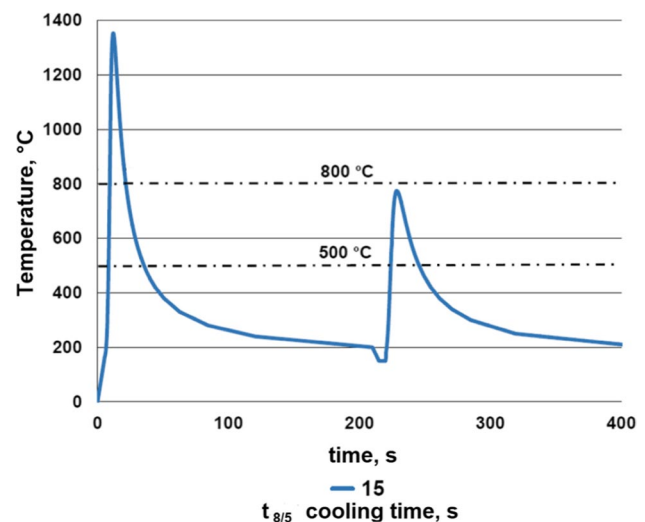


Fig. 4 ICCGAZ thermal cycle

a typical lath-like martensite microstructure is visible on the CGHAZ images. By the increase of the cooling time the grain size is larger.

In the ICHAZ during the heating period of welding thermal cycle, the austenitic transformation happens only partly; thus, a heterogeneous microstructure appears here. Figure 7 shows that the allotropic transformation has not occurred in the brighter areas, but the effect of tempering can be observed in these areas. The dark areas represent in contrast the newly formed and self-tempered martensite. For instance, on the S1100M micrographs, it is recognizable that the bright areas represent the originally elongated and tempered grains, and the dark polygonal islands at the formerly grain boundaries represent the newly formed martensite or self-tempered martensite.

In the ICCGAZ at the boundaries of the prior austenite, which was formed by the first (1350 °C peak temperature) thermal cycle, the  $\alpha$ - $\gamma$ - $\alpha$  transformation starts as the effect of the second (775 °C peak temperature) thermal cycle. The M-A (martensite-austenite) constituents at the boundaries of the grains cause local brittle zones.

After the LSCM images, field emission scanning electron microscopy (FESEM, Zeiss Sigma) was used to determine the microstructure of the investigated materials. The microstructure of the investigated base materials (BM) in delivery condition is shown in Fig. 9. The first picture shows the S960QL, the second shows the S1100M, and the third shows the S1300QL material.

As it can be seen in the pictures, in all base material samples, the microstructure is 100% martensite, which appears to be also tempered.

After the physical simulations, SEM images were not taken of all specimens. Since there are less published studies of S1300QL compared to the other two investigated



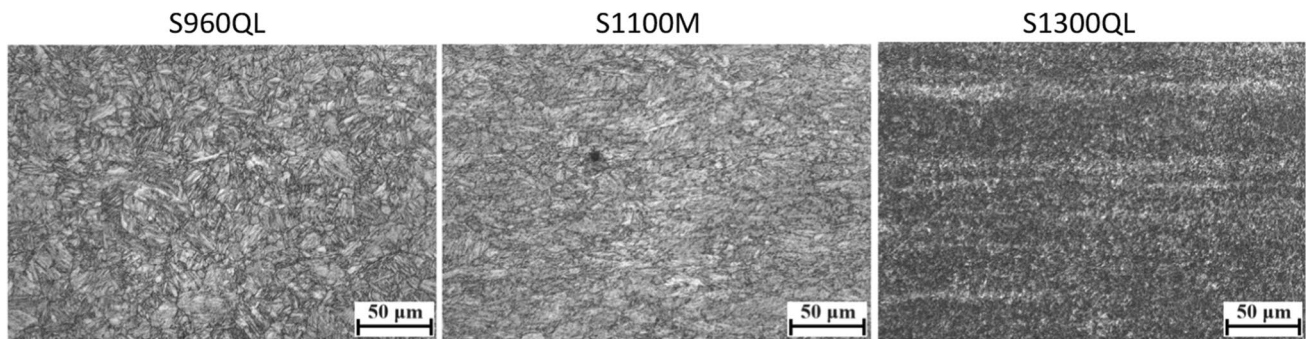


**Fig. 5** Microstructure of the base materials,  $M = \times 50$ , Nital etched

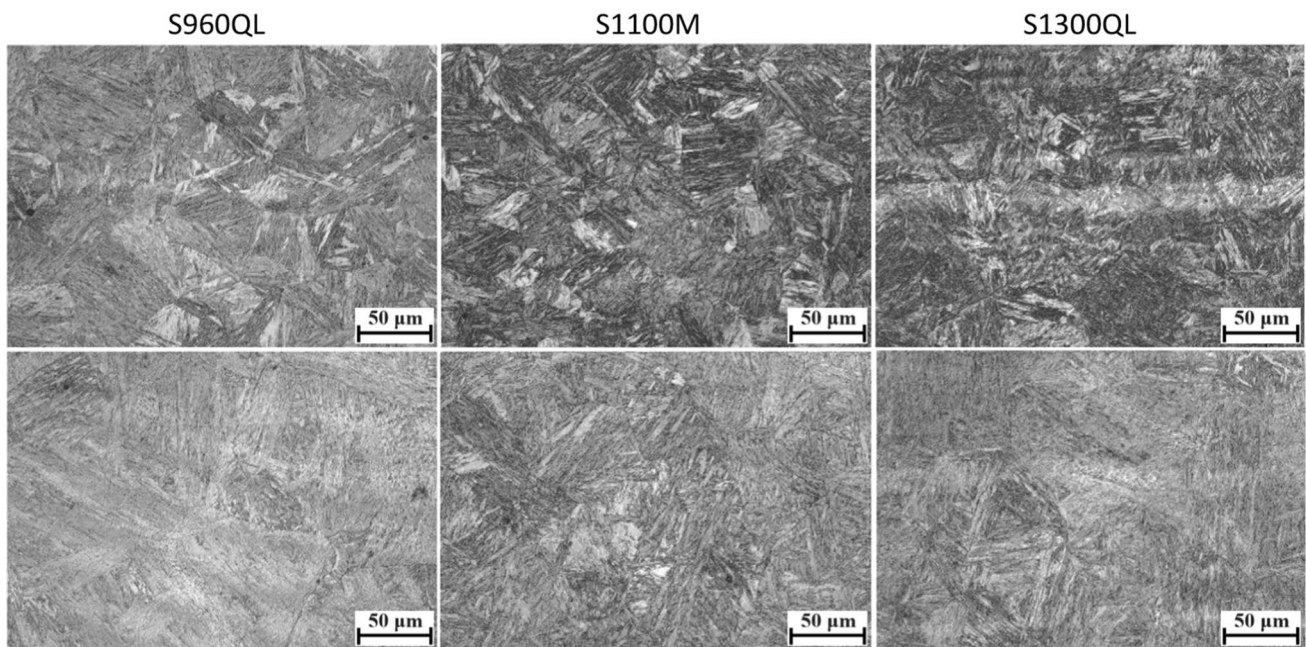


**Fig. 6** Microstructure of CGHAZ,  $T_{\max} = 1350\text{ }^{\circ}\text{C}$ ,  $M = \times 50$ , Nital etched (First row:  $t_{8/5} = 5\text{ s}$ , second row:  $t_{8/5} = 30\text{ s}$ )

steels [17–19], the deeper evaluation of the microstructure can be beneficial to understanding the results of the further hardness and impact toughness tests. Based on this, SEM images were mostly taken in the case of the CGHAZ and ICHAZ of S1300QL, and only some images as examples were made in the case of S960QL and S1100M.

The microstructure of CGHAZ of the S1300QL material belonging to the applied cooling times is shown in Fig. 10.

In the different CGHAZs, based on the SEM images with one exception (Fig. 11), all samples show that the microstructure is 100% martensite just as in the case of the investigated base materials. The auto tempering of martensite can be also identified due to the presence of small carbides in the images. In the case of S960QL with a cooling time of 30 s, the microstructure is 30% martensite and 70% bainite. It can

be also seen that the prior austenite grain size increases with increasing cooling time.

The microstructure of ICHAZ of the S1300QL material belonging to the applied cooling times are shown in Fig. 12.

In the ICHAZ region, the microstructure is basically martensitic, but with the increase of the cooling time, the carbon-depleted region (CDR) also increases. For 5 s of cooling time, the CDR is 20% (and the martensite 80%); for 15 s of cooling time, the CDR is 30% (and the martensite 70%); and for 30 s of cooling time, the CDR is about 40% (and the martensite 60%).

To make a better analysis of the ICHAZ, comparative InLens (left side in Fig. 13) and SE2 (right side in Fig. 13) images of the S1300QL material with  $t_{8/5} = 15\text{ s}$  were taken.

It can be seen that the dark regions in InLens image have reacted more with the etchant in SE2 image. This indicates



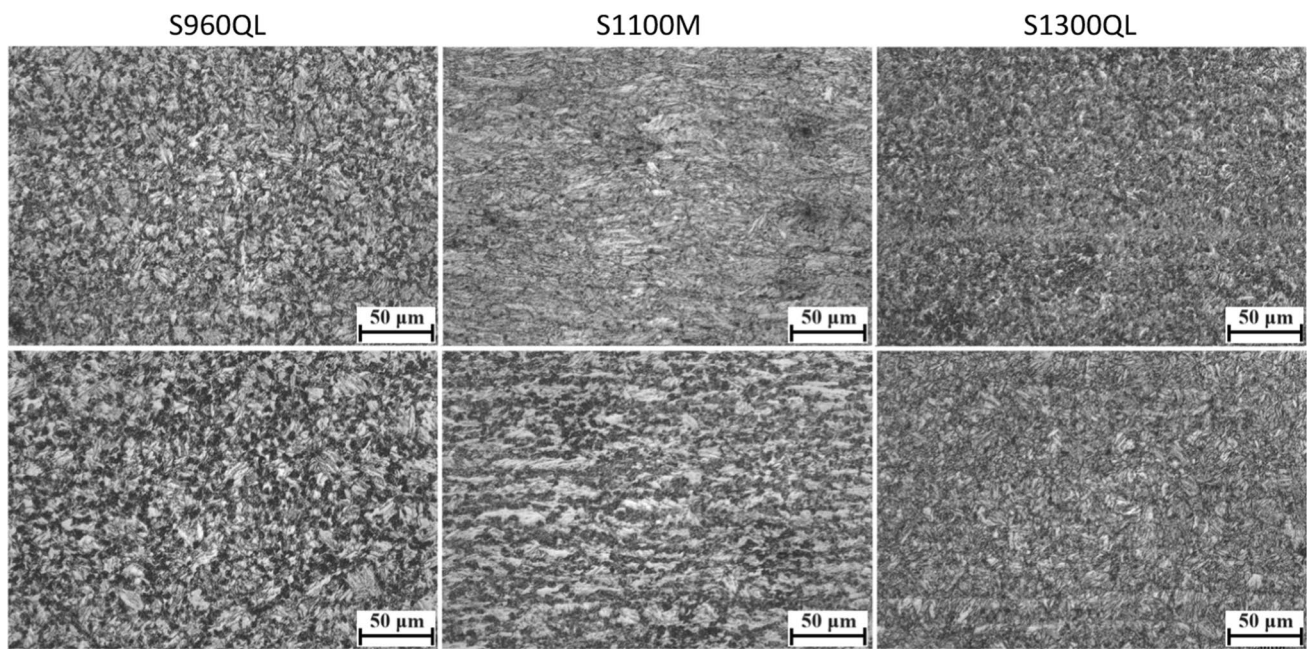


**Fig. 7** Microstructure of ICHAZ,  $T_{\max} = 775\text{ }^{\circ}\text{C}$ ,  $M = \times 50$ , Nital etched (First row:  $t_{8/5} = 5\text{ s}$ , second row:  $t_{8/5} = 30\text{ s}$ )

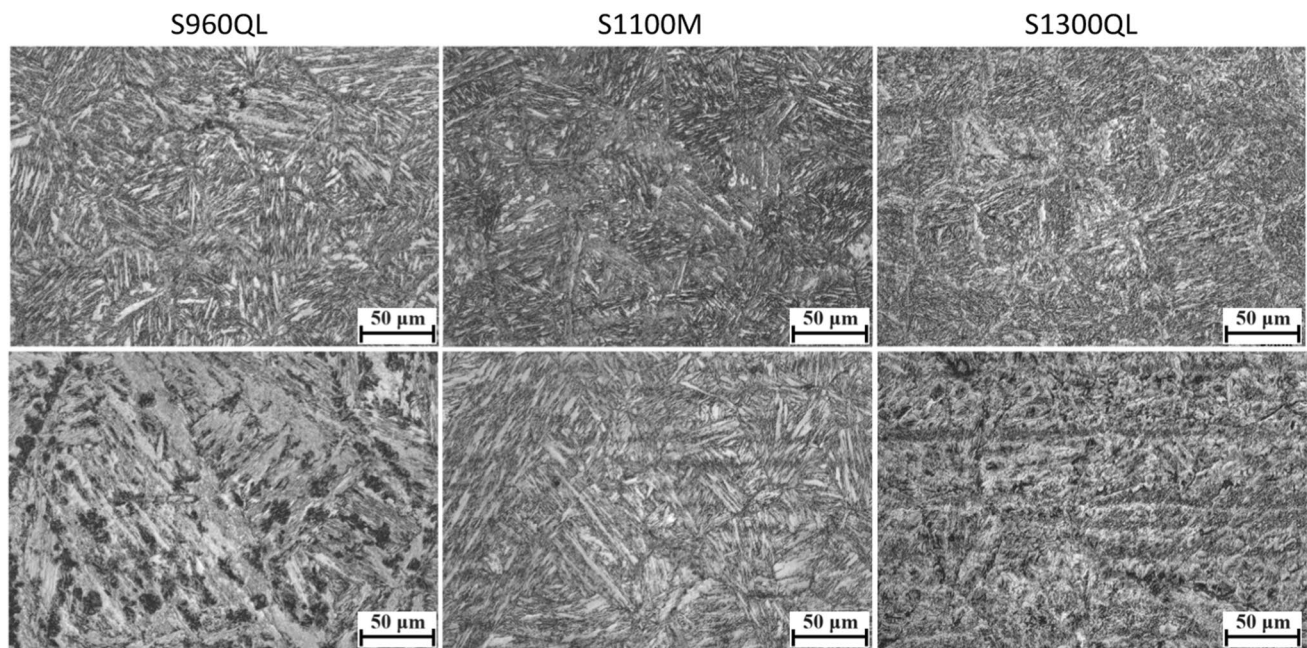


**Fig. 8** Microstructure of ICCGHAZ,  $T_{\max 1} = 1350\text{ }^{\circ}\text{C}$ ,  $T_{\max 2} = 775\text{ }^{\circ}\text{C}$ ,  $M = \times 50$ , Nital etched (First row:  $t_{8/5} = 5\text{ s}$ , second row:  $t_{8/5} = 30\text{ s}$ )

these regions have less carbon and are indeed softer than the surrounding regions.

In the ICHAZ of S1300QL with 30 s of cooling time, electron backscatter diffraction (EBSD) measurement was done as an example. A field emission scanning electron microscope (FESEM, ZEISS, SIGMA) was employed for

the EBSD measurements. In addition to the described sample preparation for SEM, an additional polishing step using  $0.04\text{ }\mu\text{m}$  colloidal silica was carried out on the EBSD samples.

The pictures in the ICHAZ after the EBSD in the case of S1300QL with  $t_{8/5} = 30\text{ s}$  can also be seen in Fig. 14.



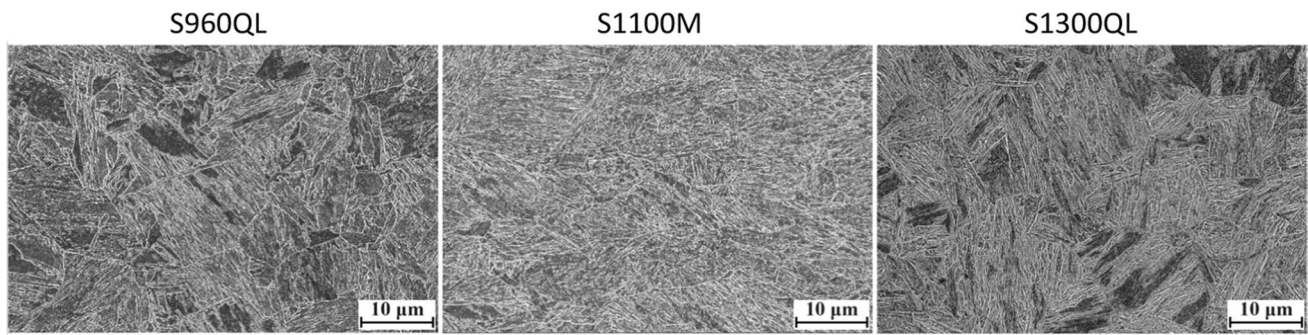


**Fig. 9** Microstructure of the base materials,  $M = \times 5000$ , Nital etched

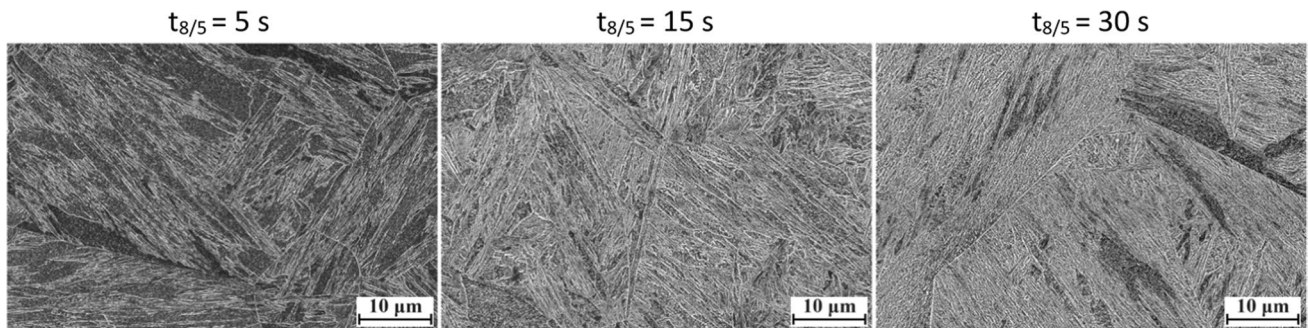


**Fig. 10** Microstructure of CGHAZ of S1300QL,  $T_{\max} = 1350$  °C,  $M = \times 5000$ , Nital etched

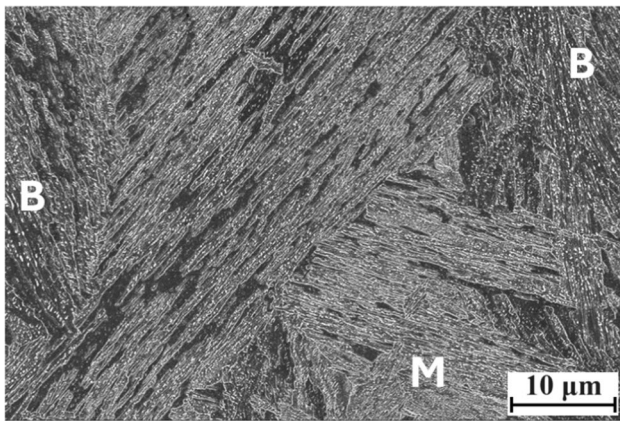


**Fig. 11** Microstructure of CGHAZ of S960QL,  $T_{\max} = 1350$  °C,  $t_{8/5} = 30$  s,  $M = \times 5000$ , Nital etched (B: bainite, M: martensite)

In the phase image, the red means BCC phases and the green means FCC phases (austenite). Therefore, there is a little retained austenite next to the carbon-depleted regions.

Retained austenite can be trapped between the small laths of martensite; however, these fine features are not visible under magnifications commonly used in SEM analysis [20]. Thus, these microstructural features are named as martensite in the case of SEM pictures since SEM was used for

microstructural evaluations. In the case of CGHAZ samples, the prior austenite grain (PAG) sizes were calculated with mean linear intercept method using a grain size calculator tool. Before the calculation, the specimens were prepared with picric acid etching and LSCM images were taken of them (e.g., Fig. 15).

The results of the PAG size calculations can be seen in Table 5. In the results the mean grain sizes were reported together with the mean standard deviations.

Based on the result of Table 5, with the increase of the cooling time, the PAG size also increases, but the reason for this growth likely is not the increase of the  $t_{8/5}$  cooling time itself, but rather the holding time above  $A_3$  temperature (which is varying in the investigated steels). As Fig. 2 shows, there are quite big differences between the simulations in this region.

### 3.2 Hardness tests

After the microscopic investigation, Vickers hardness HV10 tests were performed with a Reichert UH250 universal macro-hardness tester. In every case, five measurements were performed on all cut surfaces. The average hardness values of the different parts of the HAZ and the hardness of the base materials are presented in Figs. 16, 17, and 18.



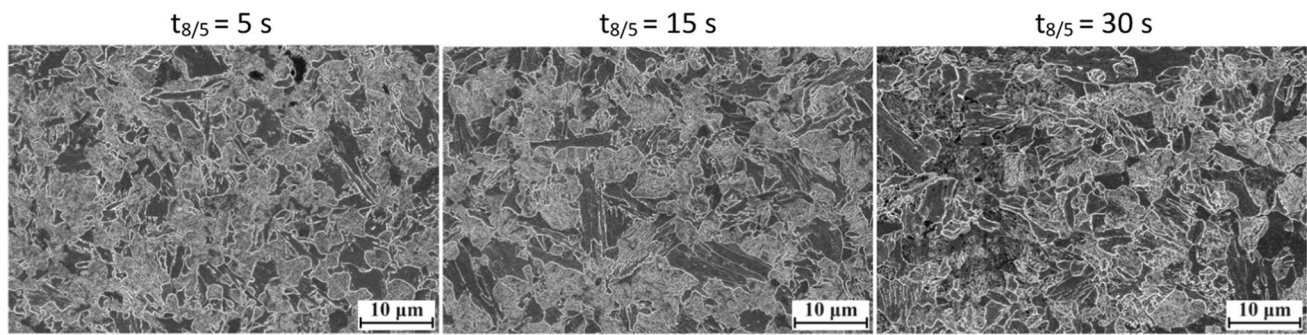


**Fig. 12** Microstructure of ICHAZ of S1300QL,  $T_{\max} = 775\text{ }^{\circ}\text{C}$ ,  $M = \times 5000$ , Nital etched

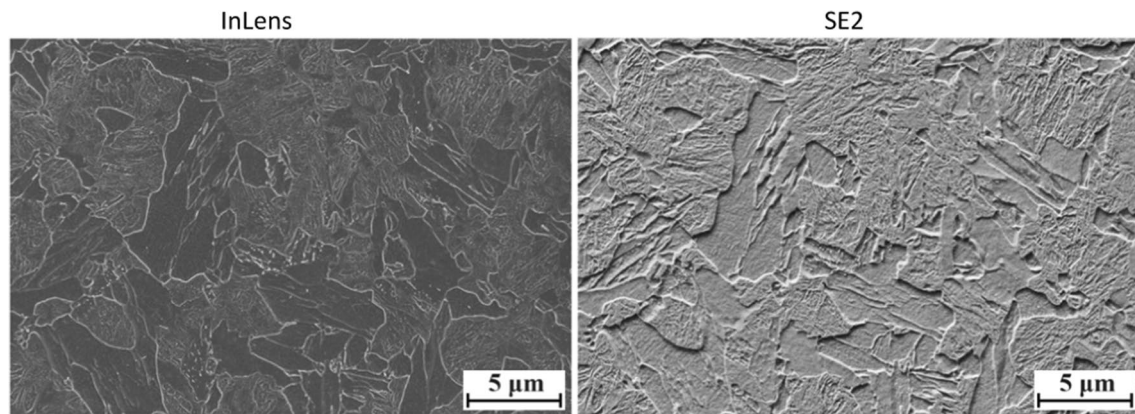


**Fig. 13** Microstructure of ICHAZ of S1300QL with InLens and SE2,  $T_{\max} = 775\text{ }^{\circ}\text{C}$ ,  $t_{8/5} = 15\text{ s}$ ,  $M = \times 10,000$ , Nital etched

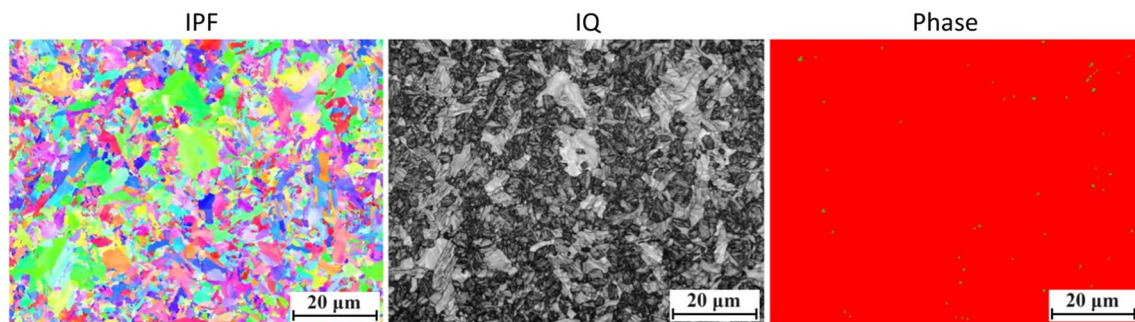


**Fig. 14** Microstructure of ICHAZ of S1300QL with inverse pole figure (IPF) (left side), image quality (IQ) (middle), and phase (right side),  $T_{\max} = 775\text{ }^{\circ}\text{C}$ ,  $t_{8/5} = 30\text{ s}$ ,  $M = \times 2500$ , polished for EBSD

Based on the results, in the case of S960QL, the hardness of the HAZ was higher than the hardness of the base material in every case, as it can be expected in the coarse-grained zone of a structural steel. Based on the results, increasing of the cooling time had a negative effect on the hardness of S960QL. For the S1100M steel, the hardness of the coarse-grained heat-affected zone was also higher than the hardness of the base material except for 30 s cooling time. Increasing the cooling time also had a negative effect on the hardness

of this material. For S1300QL, the hardness did not reach the hardness of the base material in either case; this steel was softened on account of welding heat cycles. It might be explained by the different production routes including the lack of tempering or the lower tempering temperature at S1300QL. On the contrary, S960QL and S1100M show lower base material hardness in comparison to the hardness in CGHAZ due to temper annealing at elevated (500–600  $^{\circ}\text{C}$ ) temperatures.



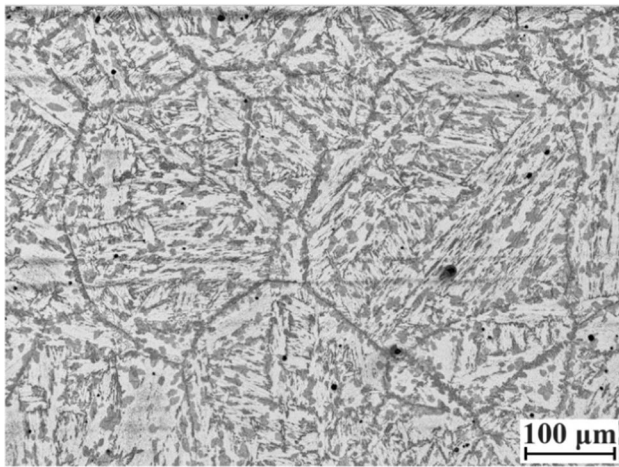


**Fig. 15** Microstructure of ICCGHAZ of S960QL with 30 s of cooling time,  $M = \times 20$ , picric acid etched

In the ICHAZ, the hardness of the specimens did not reach the hardness of the base materials. For S960QL and S1100M, the hardness reduction was not significant and increasing the cooling time did not have a major effect on the obtained values. On the other hand, the hardness of S1300QL steel ICHAZ was noticeably lower than the hardness of the base material and the hardness value decreased significantly with increasing the cooling time. It can be explained by the increasing fraction of carbon-depleted regions, which are softer than the surrounding C-rich regions.

In the ICCGHAZ, the hardness of S960QL steel is very similar both in the HAZ (with different cooling times) and in the base material. For S1100M, the hardness at 5 s cooling time slightly exceeded the hardness of the base material and a slight decrease can be observed with increasing the cooling time. The S1300QL material also softened in this zone, but the hardness slightly increased with increasing cooling time.

For a better comparison, the average value, standard deviation, and standard deviation coefficient of the hardness tests are shown in Table 6.

According to Table 6, the results obtained show acceptable standard deviation and standard deviation coefficient of the hardness values.

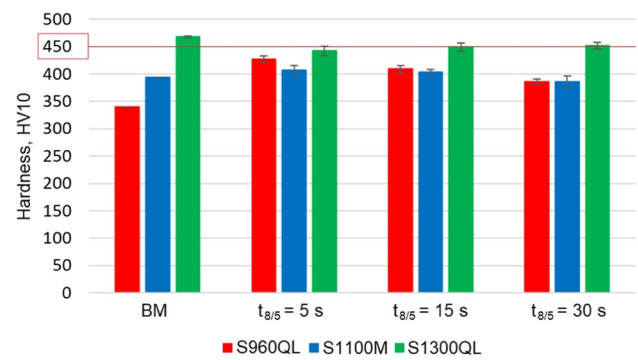


**Fig. 16** The results of the hardness tests in CGHAZ

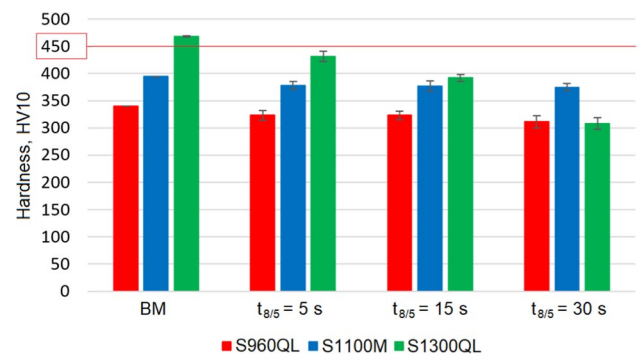


**Fig. 17** The results of the hardness tests in ICHAZ

The investigated thermomechanically controlled high-strength steel belongs to steel group 2.2 and the quenched and tempered high-strength steels belong to steel group 3.2 according to the classification of the standard ISO/TR 15608:2017 [21]. According to the requirements of EN ISO 15614-1:2017 E [22], the maximum hardness allowed for non-heat-treated steels in group 2 is 380 HV10 and in group 3 is 450 HV10. The hardness values measured on the S960QL material comply with the standard. In contrast, for S1100M, there are higher values than 380 HV10 in both CGHAZ and ICCGHAZ. In the case of S1300QL, the values in CGHAZ also exceed the specified maximum 450 HV10 hardness value. However, it should be noted that for S1100M and S1300QL, the hardness of the base material also exceeds the specified limits. The standard mentions that other values may be acceptable for materials with a yield strength greater

**Table 5** The results of the PAG size calculations

| $t_{8/5}$ cooling time, s | S960QL                       |  | S1100M                       |  | S1300QL                      |  |
|---------------------------|------------------------------|--|------------------------------|--|------------------------------|--|
|                           | Mean PAG size, $\mu\text{m}$ | Mean standard deviation, $\mu\text{m}$ | Mean PAG size, $\mu\text{m}$ | Mean standard deviation, $\mu\text{m}$ | Mean PAG size, $\mu\text{m}$ | Mean standard deviation, $\mu\text{m}$ |
| 5                         | 44.438                       | 0.341                                  | 26.663                       | 0.117                                  | 33.869                       | 0.197                                  |
| 30                        | 66.527                       | 0.387                                  | 52.214                       | 0.570                                  | 64.595                       | 0.878                                  |

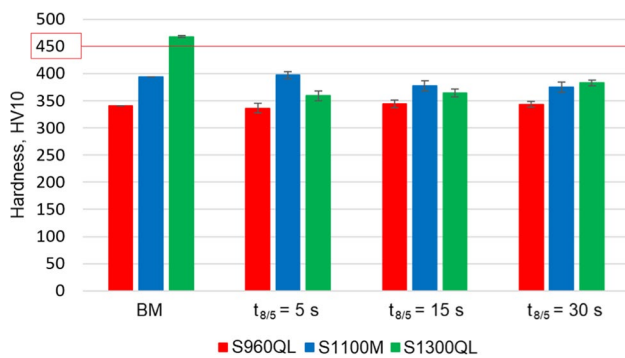


**Fig. 18** The results of the hardness tests in ICCGHAZ

than 890 MPa, but it provides no other information on what is considered acceptable.

### 3.3 Instrumented impact test

Three specimens from all the thermal cycles were used for the Charpy V-notch (CVN) impact tests, performed with PSD 300/150 instrumented equipment at  $-40^{\circ}\text{C}$ . The average CVN values of the different parts of the HAZ and the CVN values of the base materials are presented in Figs. 19, 20, and 21.

According to EN 10025–6:2019:E, the required minimum impact energy is 27 J at  $-40^{\circ}\text{C}$  for quenched and tempered steels [23]. Based on the material certificate, the investigated S960QL steel plate has 75 J CVN, although 167 J was measured during the performed impact test on the base material. According to EN 10025–4:2019 E, the required minimum impact energy is 20 J at  $-40^{\circ}\text{C}$  for thermomechanically rolled specimens [24]. Although the standards do not contain specifications for steel grades with yield strengths of 1100 MPa and 1300 MPa, the values provided in the standard are used as a reference. The results show that in CGHAZ, only S960QL material does not reach the reference value of the standard at 15 s cooling time. For S960QL and S1100M steels, the highest CVN values were obtained at 30 s cooling

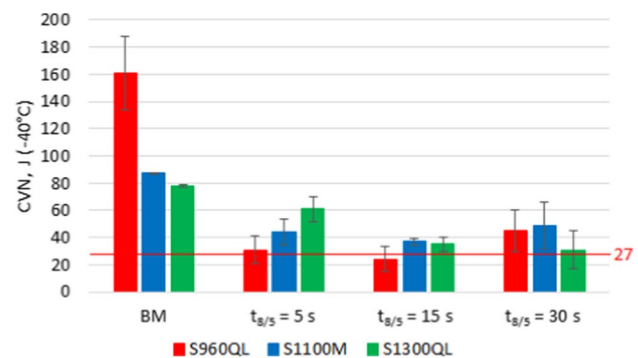


**Fig. 19** The results of Charpy V-notch impact tests in CGHAZ

time, while the lowest values were recorded at 15 s cooling time. In the case of S960QL, the presence of bainite (that was indicated by JMatPro also) may explain the better impact toughness with 30 s of cooling time compared to the samples with faster cooling. For S1300QL, the impact energy decreased continuously with increasing cooling time in accordance with the increasing PAG size from 33.8 to 64.5  $\mu\text{m}$  (Table 5).

In ICHAZ, there is a significant reduction in impact energy compared to the values obtained for the base materials due to the formation of heterogenous microstructure with brittle martensite islands. For S960QL, the CVN was less than 27 J with 30 s cooling time. For S1100M, the CVN reached 20 J in all cases, but slightly higher CVN values were measured with longer cooling times. For S1300QL, all measured values were less than 27 J and the CVN values obtained were almost equal regardless of the cooling times.

In ICCGHAZ, there is also a significant impact energy reduction. For S960QL with a cooling time of 5 s, the CVN just exceeds 27 J, but the measured values were similar in all cases. For S1100M, the CVN reaches 20 J in all cases, but the highest value was measured with 15 s cooling time. For the S1300QL, the value of 27 J is not reached in any case, but it can be observed that the impact energy is slightly reduced by increasing the cooling time. Even though the

**Table 6** The average, standard deviation, and standard deviation coefficient values of the hardness tests (where *Sd*, standard deviation; *Sdc*, standard deviation coefficient)

| HAZ  | <i>t</i> <sub>8/5</sub> , s | S960QL |       |        | S1100M |       |        | S1300QL |       |        |
|------|-----------------------------|--------|-------|--------|--------|-------|--------|---------|-------|--------|
|      |                             | HV10   | Sd, % | Sdc, % | HV10   | Sd, % | Sdc, % | HV10    | Sd, % | Sdc, % |
| CG   | 5                           | 427    | 5.77  | 1.35   | 407    | 8.76  | 2.15   | 442     | 9.03  | 1.94   |
|      | 15                          | 409    | 6.83  | 1.67   | 403    | 8.14  | 2.02   | 449     | 7.3   | 1.63   |
|      | 30                          | 386    | 4.25  | 1.1    | 386    | 11.63 | 3.01   | 452     | 5.26  | 1.16   |
| IC   | 5                           | 323    | 8.34  | 2.58   | 378    | 7.4   | 1.96   | 431     | 6.46  | 1.5    |
|      | 15                          | 323    | 5.43  | 1.68   | 377    | 9.22  | 2.45   | 392     | 9.26  | 2.36   |
|      | 30                          | 311    | 10.99 | 3.53   | 375    | 6.54  | 1.74   | 308     | 9.68  | 3.14   |
| ICCG | 5                           | 336    | 8.9   | 2.65   | 397    | 9.47  | 2.39   | 359     | 8.81  | 2.45   |
|      | 15                          | 344    | 7.61  | 2.21   | 377    | 6.47  | 1.71   | 364     | 6.84  | 1.88   |
|      | 30                          | 343    | 5.92  | 1.73   | 375    | 10.29 | 2.75   | 383     | 5.46  | 1.42   |



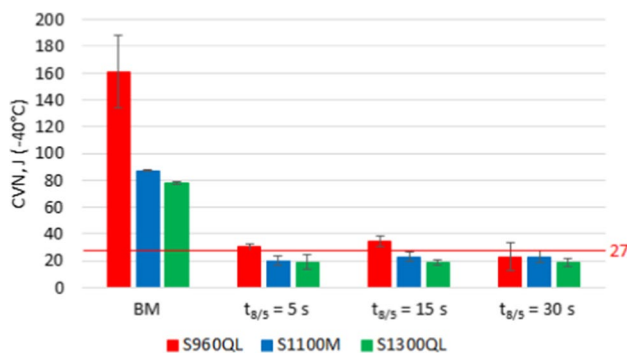


**Fig. 20** The results of Charpy V-notch impact tests in ICHAZ

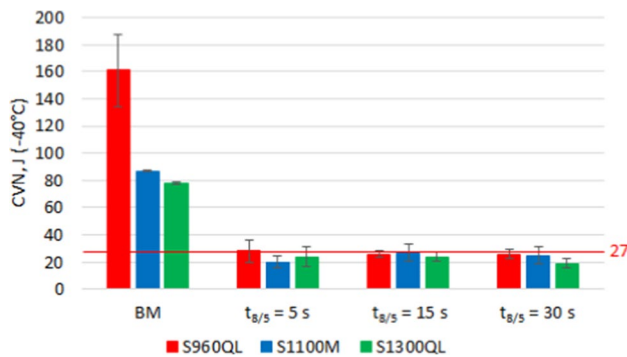


**Fig. 21** The results of Charpy V-notch impact tests in ICCGHAZ

martensite is tempered in this local subzone, a drastic reduction in toughness occurs due to the large PAG size and the brittle martensite islands that form at the grain boundaries in the second heat cycle.

For a better overview, the average values, standard deviation, and standard deviation coefficient of CVN are shown in Table 7.

According to Table 7, the results obtained show acceptable standard deviation and standard deviation coefficient

of the CVN values. The measured lateral expansion values in the function of impact energy are summarized in Fig. 22.

Instrumented impact toughness testing can provide more detailed information about the fracture process and the ductile/brittle behavior of the material compared to the traditional Charpy V-notch impact toughness test, which only determines the total energy absorbed during the fracture. The load-time diagram can be determined by using strain gauge measurement technology, and the characteristic points of the fracture process can be identified. From the load-time diagram, the force–displacement diagram can be calculated. An example for force–displacement diagram is presented in Fig. 23. Assuming that the crack initiation occurs at the maximal force, the registered diagram can be divided into two parts according to the maximal force. Until the maximum force, the area under the curve is considered the absorbed energy for crack initiation ( $W_i$ ), while the remaining area is for crack propagation ( $W_p$ ). As the ratio of the absorbed energy for the crack initiation increases, the toughness of the examined material reduces [13, 25, 26].

The force–displacement diagrams of the base materials and the examined parts of the HAZ in the case of 5 and 30 s of colling time can be seen in Figs. 24, 25, 26, 27, 28, 29, and 30. In the first column, the pictures show the S960QL; in the second column, the pictures show the S1100M; and in the third column, the pictures show the S1300QL material.

The diagrams clearly demonstrate the significant difference between the different material qualities. It is also noticeable that the higher the yield strength of the material tested, the more brittle it behaves. The difference between the maximum forces is also noticeable, which is clearly the highest at S1300QL due to the highest strength. In this case, because there will be a larger area under the curve, the maximum force is higher, while the toughness will not actually be better.

After the instrumented Charpy V-notch impact toughness tests, force–displacement diagrams were determined and

**Table 7** The average, standard deviation, and standard deviation coefficient values of CVN (where  $Sd$ , standard deviation;  $Sdc$ , standard deviation coefficient)

| HAZ  | $t_{8/5}$ , s | S960QL             |       |        | S1100M             |       |        | S1300QL            |       |        |
|------|---------------|--------------------|-------|--------|--------------------|-------|--------|--------------------|-------|--------|
|      |               | CVN, J<br>(−40 °C) | Sd, % | Rsd, % | CVN, J<br>(−40 °C) | Sd, % | Rsd, % | CVN, J<br>(−40 °C) | Sd, % | Rsd, % |
| CG   | 5             | 31                 | 10.01 | 32.32  | 44                 | 9.54  | 21.68  | 61                 | 9.54  | 15.64  |
|      | 15            | 24                 | 9.28  | 39.26  | 37                 | 2.47  | 6.64   | 35                 | 5.68  | 16.46  |
|      | 30            | 45                 | 15.01 | 33.42  | 49                 | 17.04 | 34.54  | 31                 | 14.08 | 46.16  |
| IC   | 5             | 30                 | 2.85  | 9.63   | 20                 | 3.28  | 16.39  | 19                 | 5.77  | 29.86  |
|      | 15            | 34                 | 3.99  | 11.81  | 23                 | 3.12  | 13.58  | 19                 | 2.02  | 10.83  |
|      | 30            | 23                 | 10.37 | 44.69  | 23                 | 4.16  | 18.37  | 19                 | 3.01  | 16.15  |
| ICCG | 5             | 28                 | 8.49  | 29.91  | 20                 | 4.33  | 21.65  | 24                 | 7.00  | 29.17  |
|      | 15            | 26                 | 2.02  | 7.79   | 27                 | 6.59  | 26.21  | 24                 | 3.50  | 14.89  |
|      | 30            | 26                 | 3.08  | 10.43  | 25                 | 6.05  | 24.36  | 19                 | 3.50  | 18.92  |

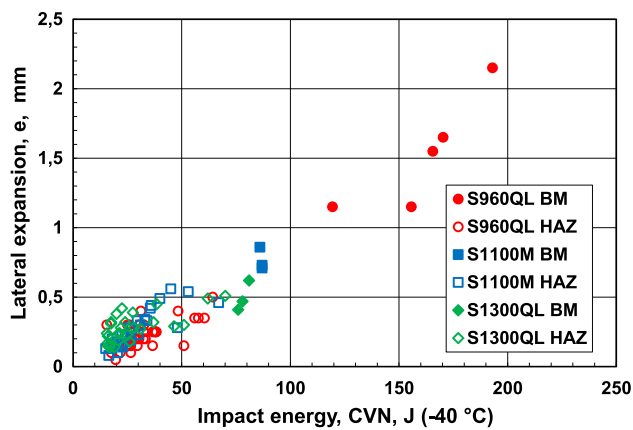


**Fig. 22** Lateral expansion values in the function of impact energy in BM and HAZ

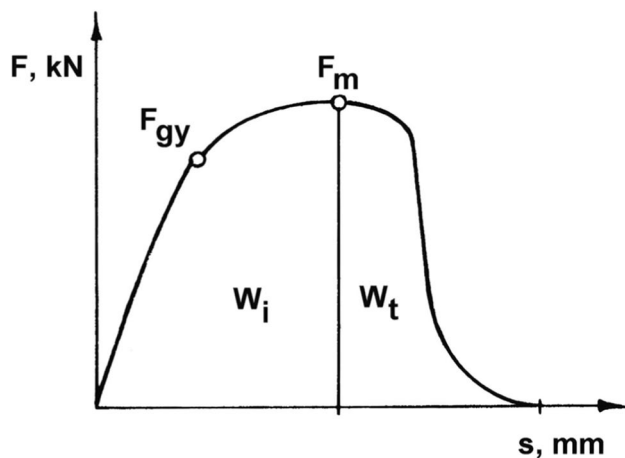


**Fig. 23** Force–displacement diagram of the base materials

the absorbed energy for crack initiation was also calculated (Table 8).

The values of Table 8 indicate the brittle behavior of the investigated HAZ areas, where mostly unstable crack

propagation can be seen in all diagrams. For S960QL, according to the values in CGHAZ seems more brittle than ICHAZ, although the difference is minimal. The  $t_{8/5}$  cooling time did not significantly affect the ratio of  $W_i$  in the examined interval. For S1100M, CGHAZ showed the less brittle behavior compared to ICHAZ and ICCGAZ. In this area,  $W_i$  increased with increasing cooling time. In the case of S1300QL, it can be detected that every investigated subzone was also totally brittle, almost independently from the set of  $t_{8/5}$  cooling time. The shorter cooling time had a positive result for the  $W_i$  values, except in the ICHAZ.

Since the results show a large degradation of the mechanical properties in the tested heat-affected zones, reducing the extent of it could be beneficial. Electron beam welding can be an advantageous technology for minimizing the extension of critical HAZ subzones; furthermore, post-weld heat treatment (PWHT) can improve the mechanical properties of the weld and the HAZ [27].

## 4 Conclusions

The CGHAZ, ICHAZ, and ICCGAZ of the investigated S960QL, S1100M, and S1300QL high-strength structural steels were successfully simulated for three technological variants by Gleeble 3500 physical simulator. After the successfully simulated heat cycles, specimens were prepared for microscopic examination, hardness, and instrumented Charpy V-notch impact toughness tests. After the investigations, the following conclusions can be obtained:

- Based on the laser scanning confocal microscope and scanning electron microscope images, the microstructure of all investigated base materials is tempered martensite. In the different CGHAZs with one exception where the microstructure is 30% martensite and 70% bainite (S960QL with  $t_{8/5} = 30$  s), the microstructure is 100% tempered martensite just as in the case of the base materials. In the ICHAZ during the heating period of welding

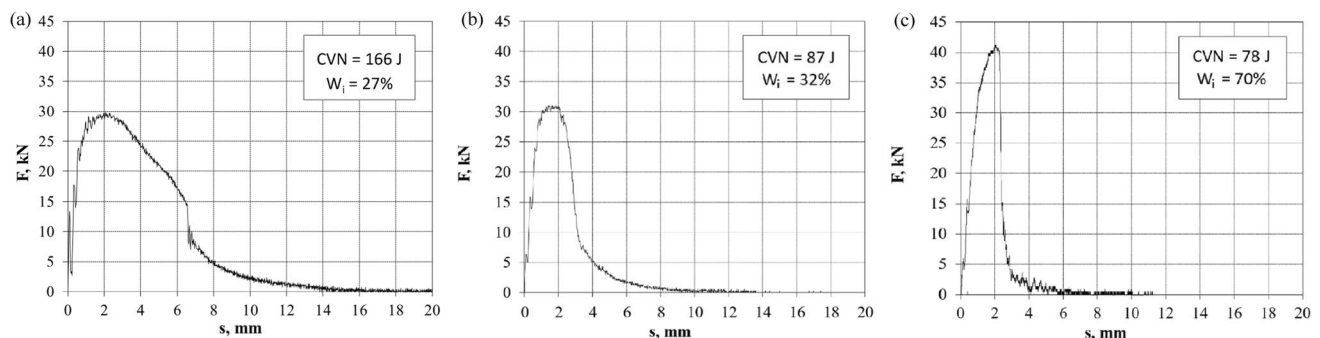


**Fig. 24** Force–displacement diagrams of the base materials: **a** S960QL, **b** S1100M, **c** S1300QL



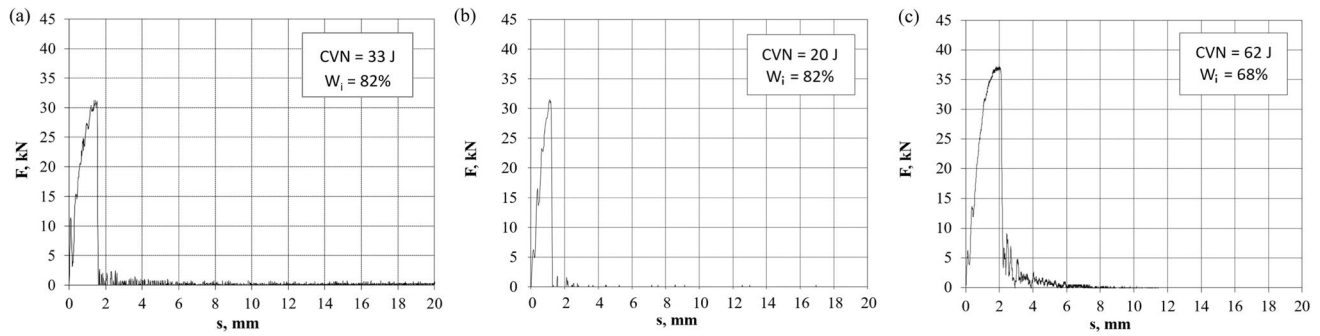


**Fig. 25** Force–displacement diagrams of the CGHAZ with 5 s of  $t_{8/5}$  cooling time: **a** S960QL, **b** S1100M, **c** S1300QL

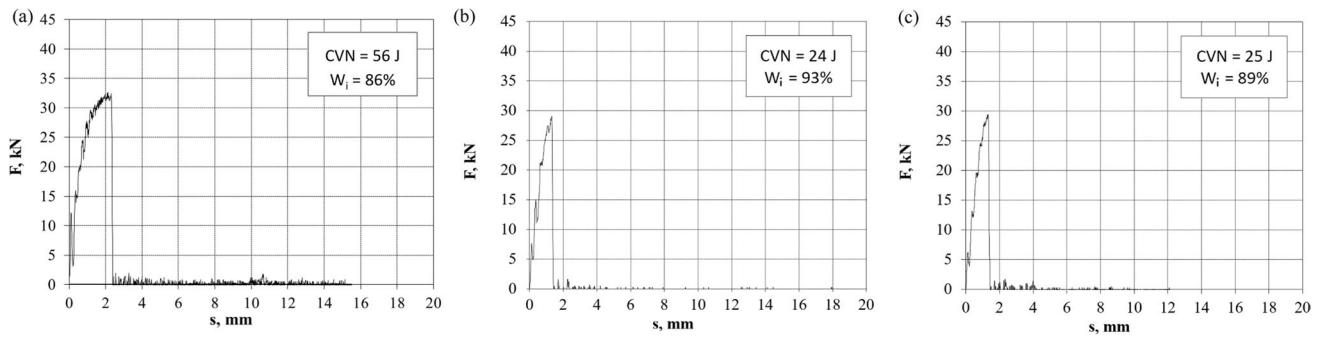


**Fig. 26** Force–displacement diagrams of the CGHAZ with 30 s of  $t_{8/5}$  cooling time: **a** S960QL, **b** S1100M, **c** S1300QL

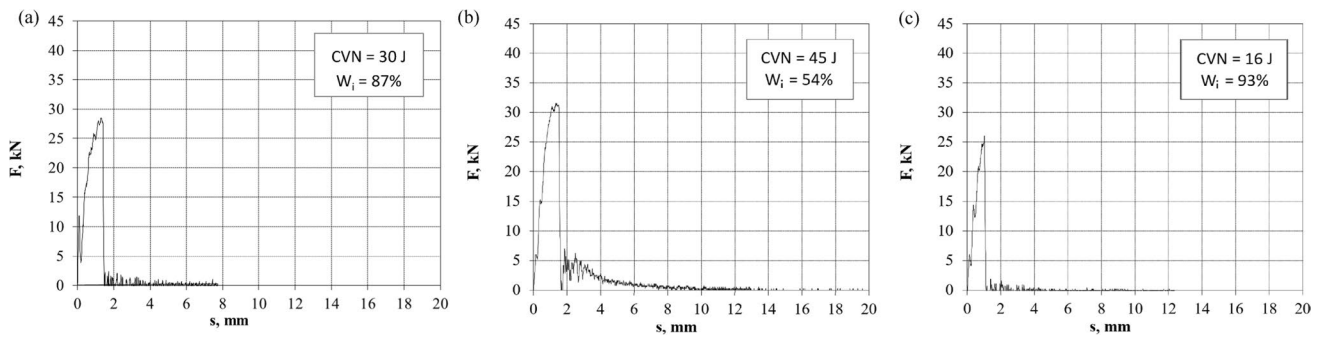


**Fig. 27** Force–displacement diagrams of the ICHAZ with 5 s of  $t_{8/5}$  cooling time: **a** S960QL, **b** S1100M, **c** S1300QL

thermal cycle, the austenitic transformation occurs only partly; thus, a heterogeneous microstructure appears here in every cases. In the case of S1300QL in the ICHAZ region, the microstructure is basically martensitic, but with the increase of the cooling time, the carbon-depleted region (CDR) also increases. For 5 s of cooling time, the CDR is 20%; for 15 s of cooling time, the CDR is 30%; and for 30 s of cooling time, the CDR is about 40%. Furthermore, based on the results of the electron backscatter diffraction in this zone, there is a little retained austenite or M-A constituents next to the carbon-depleted regions.

In ICCGAZ, the typical martensitic microstructure can be detected despite the tempering process in the case of all three materials. In the case of CGHAZ samples, the prior austenite grain (PAG) sizes were also calculated. Based on the results, with the increase of the cooling time, the PAG size also increases, but the reason for this growth probably is not the increase of the  $t_{8/5}$  cooling time itself, but rather the holding time above  $A_3$  temperature.

- On the basis of hardness measurements, in the case of S960QL, the hardness of the HAZ was greater than the

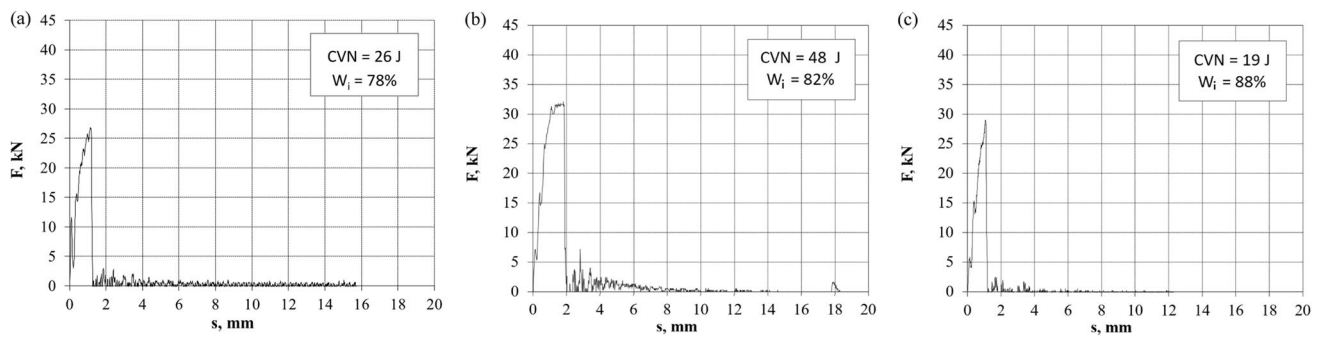


**Fig. 28** Force–displacement diagrams of the ICHAZ with 30 s of  $t_{8/5}$  cooling time: **a** S960QL, **b** S1100M, **c** S1300QL

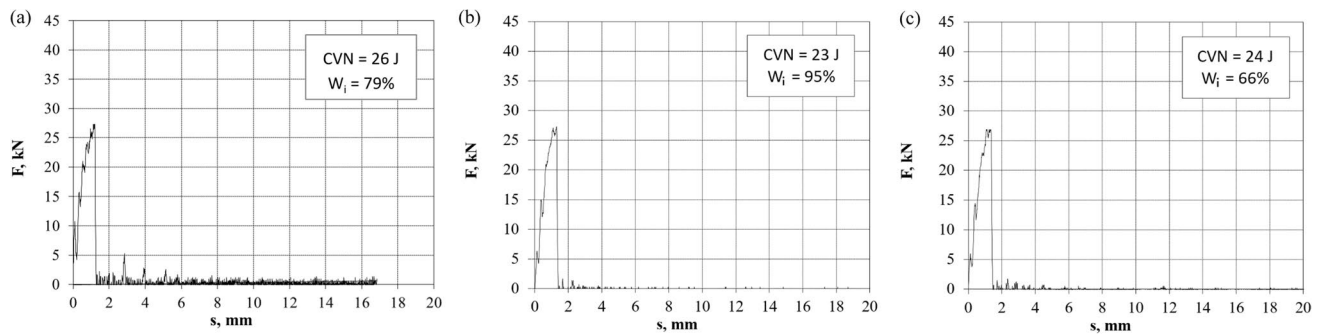


**Fig. 29** Force–displacement diagrams of the ICCGHAZ with 5 s of  $t_{8/5}$  cooling time: **a** S960QL, **b** S1100M, **c** S1300QL

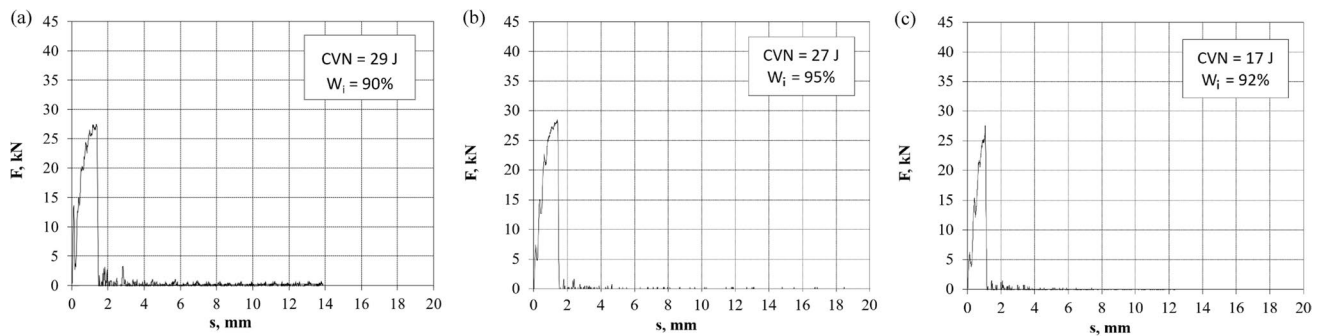


**Fig. 30** Force–displacement diagrams of the ICCGHAZ with 30 s of  $t_{8/5}$  cooling time: **a** S960QL, **b** S1100M, **c** S1300QL

**Table 8** The absorbed energy for crack initiation

| HAZ areas     | The absorbed energy for crack initiation, % |               |     |     |                |               |     |     |                |               |     |     |
|---------------|---|---------------|-----|-----|----------------|---------------|-----|-----|----------------|---------------|-----|-----|
|               | S960QL                                      |               |     |     | S1100M         |               |     |     | S1300QL        |               |     |     |
|               | Delivery state                              | $t_{8/5}$ , s |     |     | Delivery state | $t_{8/5}$ , s |     |     | Delivery state | $t_{8/5}$ , s |     |     |
|               |   | 5             | 15  | 30  |                | 5             | 15  | 30  |                | 5             | 15  | 30  |
| Base material | 28  | N/A           | N/A | N/A | 37             | N/A           | N/A | N/A | 69             | N/A           | N/A | N/A |
| CG            | N/A   | 88            | 92  | 86  | N/A            | 56            | 69  | 71  | N/A            | 72            | 84  | 85  |
| IC            | N/A   | 87            | 81  | 78  | N/A            | 84            | 82  | 90  | N/A            | 92            | 87  | 84  |
| ICCG          | N/A   | 79            | 83  | 90  | N/A            | 95            | 88  | 89  | N/A            | 79            | 79  | 87  |



- hardness of the base material in every case. It can be also noted that increasing the cooling time had a negative effect on the hardness of S960QL and S1100M. After the simulation, the S1300QL material had a lower hardness than the base material, and the differences in the measured hardness values at different cooling times were almost negligible. In the ICHAZ, the hardness of the specimens did not reach the hardness of the base materials. For S960QL and S1100M, the hardness reduction was not significant. On the other hand, the hardness of S1300QL steel was noticeably lower than the hardness of the base material and the hardness value decreased significantly with increasing cooling time. In the ICCGHAZ, the measured hardness of S960QL steel is very similar both in the heat-affected zone (with different cooling times) and in the base material. For S1100M, the hardness at 5 s cooling time slightly exceeded the hardness of the base material and a slight decrease can be observed with increasing cooling time. The S1300QL material also softened in this zone, but the hardness slightly increased with increasing cooling time. Based on the microstructural images, the fraction of carbon-depleted regions increases along with increasing  $t_{8/5}$  time, leading to decrease the hardness in ICHAZ samples of S1300QL.
- The results of the impact tests show that in CGHAZ, only S960QL material does not reach the reference value (27 J at  $-40\text{ }^{\circ}\text{C}$ ) of the standard at 15 s cooling time. For S960QL and S1100M steels, the highest CVN values were obtained at 30 s cooling time, while the lowest values were recorded at 15 s cooling time. In the case of S960QL, the increased fraction of bainite may explain the better impact toughness with 30 s of cooling time compared to the samples with faster cooling. For S1300QL, the impact energy decreased continuously with increasing cooling time. In ICHAZ, a significant reduction can be obtained in impact energy compared to the values obtained for the base materials. For S960QL, the CVN was less than 27 J with 30 s cooling time. For S1100M, the CVN reached 20 J in all cases, but slightly higher CVN values were measured with longer cooling times. For S1300QL, all measured values were less than 27 J and the CVN values obtained were almost equal regardless of the cooling times. In ICCGHAZ, there is also a significant impact energy reduction. For S960QL with a cooling time of 5 s, the CVN just exceeds 27 J, but the measured values were similar in all cases. For S1100M, the CVN reaches 20 J in all cases, but the highest value was measured with 15 s cooling time. For the S1300QL, the value of 27 J is not reached in any case, but it can be observed that the impact energy is slightly reduced by increasing the cooling time.
  - Based on the absorbed energy for crack initiation, the calculated values indicate the brittle behavior of the investigated HAZ areas, where mostly unstable crack propagation can be seen in all diagrams. For S960QL, according to the values in CGHAZ seems more brittle than ICHAZ, although the difference is negligible. The  $t_{8/5}$  cooling time did not significantly affect the ratio of  $W_i$  in the examined interval. For S1100M, CGHAZ showed the least brittle behavior among all materials and all subzones. In this area,  $W_i$  increased with increasing cooling time. In the case of S1300QL, it can be detected that every investigated subzone was totally brittle, almost independently from the set of  $t_{8/5}$  cooling time. The shorter cooling time had a positive result for the  $W_i$  values, except in the ICHAZ.
  - Overall, the test results show that the application of shorter  $t_{8/5}$  cooling time can be beneficial for the investigated high-strength steel grades, since significant toughness reduction and the risk of softening occur in the whole cooling time range.

**Acknowledgements** Dr. Tervo and Dr. Kaijalainen are grateful to the funding of the research program FOSSA – Fossil Free Steel Applications (Dno. 5397/31/2021).

**Funding** Open access funding provided by University of Miskolc. The participation in the 76th IIW Annual Assembly and International Conference was supported by the Hungarian Welding Society (MAHEG), the MHE Foundation, and the Flexman Robotics Ltd. This paper has been supported by the János Bolyai Research Scholarship of the Hungarian Academy of Sciences (Grant number: Bo/00643/22/6).

## Declarations

**Conflict of interest** The authors declare no competing interests.

**Open Access** This article is licensed under a Creative Commons Attribution 4.0 International License, which permits use, sharing, adaptation, distribution and reproduction in any medium or format, as long as you give appropriate credit to the original author(s) and the source, provide a link to the Creative Commons licence, and indicate if changes were made. The images or other third party material in this article are included in the article's Creative Commons licence, unless indicated otherwise in a credit line to the material. If material is not included in the article's Creative Commons licence and your intended use is not permitted by statutory regulation or exceeds the permitted use, you will need to obtain permission directly from the copyright holder. To view a copy of this licence, visit <http://creativecommons.org/licenses/by/4.0/>.

## References

1. Lahtinen T, Vilaca P, Peura P, Mehtonen S (2019) MAG welding tests of modern high strength steels with minimum yield strength of 700 MPa. Appl Sci 9:1031. <https://doi.org/10.3390/app9051031>
2. Jha RN, Dutta K, Ray KK (2010) Effect of tempering on mechanical properties of V-added AISI 4335 steel. ISIJ Int 50(4):607–612

3. Shi ZM, Liu K, Wang MQ (2012) Effect of tensile deformation of austenite on the morphology and strength of lath martensite. *Met Mater Int* 18(2):317–320. <https://doi.org/10.3390/app10072205>
4. St. Węglowski M, Zeman M, Lomozik M (2013) Physical simulation of weldability of Weldox 1300 steel, *Materials Science Forum*, 762, pp. 551–555. <https://doi.org/10.4028/www.scientific.net/MSF.762.551>
5. St. Węglowski M, Zeman M (2013) Prevention of cold cracking in ultra-high strength steel Weldox 1300, *Archives of civil and mechanical engineering*, 163, <https://doi.org/10.1016/j.acme.2013.10.010>
6. Tümer M, Pixner F, Enzinger N (2021) Residual stresses, microstructure, and mechanical properties of electron beam welded thick S1100 steel, *J Mater Eng Perform* <https://doi.org/10.1007/s11665-021-06348-1>
7. Chen M-T, Cai A, Pandey M, Shen C, Zhang Y, Hu L (2023) Mechanical properties of high strength steels and weld metals at arctic low temperatures. *Thin-walled structures* 185:110543. <https://doi.org/10.1016/j.tws.2023.110543>
8. Ilic A, Miletic I, Nikolic RR, Marjanovic V, Ulewicz R, Stojanovic B, Ivanovic L (2020) Analysis of influence of the welding procedure on impact toughness of welded joints of the high-strength low-alloyed steels. *Appl Sci* 10:2205
9. Dunne DP, Pang W (2017) Displaced hardness peak phenomenon in heat-affected zone of welded quenched and tempered EM812 steel. *Weld World* 61:57–67
10. Hoehauser F, Ernst W, Rauch R, Vallant R, Enzinger N (2012) Influence of the soft zone on the strength of welded modern HSLA steels. *Weld World* 56:77–85
11. Olsson L, Siewert D, Liu TA, Edwards S, Handbook GRASM (1995) welding brazing and soldering; ASM International: Nov- elty. OH, USA, pp 191–212
12. Nevasmaa P (1996) Evaluation of HAZ toughness properties in modern low carbon low impurity 420, 550 and 700 MPa yield strength thermomechanically processed steels with emphasis on local brittle zones; Lisensiaatintyö. University of Oulu, Oulu, Finland
13. Gáspár M (2019) Effect of welding heat input on simulated HAZ areas in S960QL high strength steel. *Metals* 9:1226. <https://doi.org/10.3390/met9111226>
14. European Committee for Standardization (2004) Hot rolled products of structural steels – Part 1: General technical delivery conditions. EN 10025–1:E
15. Laitinen R, Porter DA, Karjalainen LP, Leiviskä P, Kömi J (2013) Physical simulation for evaluating heat-affected zone toughness of high and ultra-high strength steels. *Mater Sci Forum* 762:711–716. <https://doi.org/10.4028/www.scientific.net/MSF.762.711>
16. Mičian M, Winczek J, Harmaniak D, Koňár R, Gucwa M, Moravec J (2021) Physical simulation of individual heat-affected zones in S960MC steel. *Arch Metall Mater* 66(1):81–89. <https://doi.org/10.24425/amm.2021.134762>
17. Ghafouri M, Afkhami S, Pokka AP, Javaheri V, Togiani A, Larkiola J, Björk T (2024) Effect of temperature on the plastic flow and strain hardening of direct-quenched ultra-high strength steel S960MC. *Thin-Walled Struct* 194(A):111319. <https://doi.org/10.1016/j.tws.2023.111319>
18. Keranen L, Nousiainen O, Javaheri V, Kaijalainen A, Pokka AP, Keskitalo M, Niskanen J, Kurvinen E (2022) Mechanical properties of welded ultrahigh-strength S960 steel at low and elevated temperatures. *J Constr Steel Res* 198:107517. <https://doi.org/10.1016/j.jcsr.2022.107517>
19. Amraei M, Afkhami S, Javaheri V, Larkiola J, Skriko T, Björk T, Zhao XL (2020) Mechanical properties and microstructural evaluation of the heat-affected zone in ultra-high strength steels. *Thin-Walled Structures* 157:107072. <https://doi.org/10.1016/j.tws.2020.107072>
20. Afkhami S, Javaheri V, Amraei M, Skriko T, Piili H, Zhao XL, Björk T (2022) Thermomechanical simulation of the heat-affected zones in welded ultra-high strength steels: microstructure and mechanical properties. *Mater Des* 213:110336. <https://doi.org/10.1016/j.matdes.2021.110336>
21. International Organization for Standardization (2017) Welding. Guidelines for a metallic materials grouping system, ISO/TR, p 15608
22. European Committee for Standardization (2017) Specification and qualification of welding procedures for metallic materials – welding procedure test – Part 1: Arc and gas welding of steels and arc welding of nickel and nickel alloys. EN ISO 15614–1:E
23. European Committee for Standardization (2019) Hot rolled products of structural steels – Part 6: Technical delivery conditions for flat products of high yield strength structural steels in the quenched and tempered condition. EN 10025–6:E
24. European Committee for Standardization (2019) Hot rolled products of structural steels – Part 4: Technical delivery conditions for thermomechanical rolled weldable fine grain structural steels. EN 10025–4:E
25. Gyöngyvér L. B, Winkler S, Tóth L, Blauel JG (1997) Investigations on the brittle to ductile fracture behaviour of base metal, weld metal and HAZ material by instrumented impact testing, In *Proceedings of the 1st International Conference on Welding Technology, Materials and Material Testing, Fracture Mechanics and Quality Management*. Wien, Austria, pp 423–432
26. Gáspár M, Sisodia R (2018) Improving the HAZ toughness of Q+T high strength steels by post weld heat treatment, *IOP Conference Series, Mater Sci Eng* 426, Paper: 012012, <https://doi.org/10.1088/1757-899X/426/1/012012>
27. Sisodia R, Węglowski M, Sliwinski P (2024) In situ localised post-weld heat treatment with electron beam welding of S690QL steel. *J Adv Join Process* 9:100182. <https://doi.org/10.1016/j.jajp.2023.100182>

**Publisher's Note** Springer Nature remains neutral with regard to jurisdictional claims in published maps and institutional affiliations.